



Universidad Autónoma  
de Madrid

**Biblos-e Archivo**  
Repositorio Institucional UAM

**Repositorio Institucional de la Universidad Autónoma de Madrid**  
<https://repositorio.uam.es>

Esta es la **versión de autor** del artículo publicado en:  
This is an **author produced version** of a paper published in:

Materials Science and Engineering: B 271 (2021): 115271

**DOI:** <https://doi.org/10.1016/j.mseb.2021.115271>

**Copyright:** © 2021 Elsevier B.V.

El acceso a la versión del editor puede requerir la suscripción del recurso  
Access to the published version may require subscription

**Bringing immuno-assemblies to optoelectronics; sandwich assay integration of a nanostructured porous-silicon/gold-nanoparticle phototransistor**

*Rehab Ramadan<sup>1,2,&</sup>, Chloé Rodriguez<sup>1,3,&</sup>, Vicente Torres-Costa<sup>1</sup>, Valerio Pini<sup>3</sup>, Raul José Martín Palma<sup>1</sup>, Virginia Cebrián<sup>3</sup>, Rodrigo Calvo Membibre<sup>1,3</sup>, Oscar Ahumada<sup>3</sup>, Miguel Manso Silván<sup>1,4 \*</sup>*

1 Departamento de Física Aplicada and Instituto de Ciencia de Materiales Nicolás Cabrera, Universidad Autónoma de Madrid, 28049 Madrid, Spain.

2 Department of Physics, Faculty of Science, Minia University, 61519 Minia, Egypt.

3 Mecwins S.A., Ronda de Poniente 15 2ºD, 28760 Tres Cantos, Madrid.

4 Centro de Microanálisis de Materiales, Universidad Autónoma de Madrid, 28049 Madrid, Spain.

&, authors with equal contributions.

\*corresponding author: miguel.manso@uam.es, tel: +34 914974918

## **Abstract**

The exquisite specificity of biomolecular interactions can be used to integrate photonic and electronic components into nanomaterial-based architectures. In this line, a field-effect phototransistor based on Si/porous silicon (PSi) structures was fabricated by quantitatively attaching Gold nanoparticles (AuNPs) to the PSi surface by an immunoassay. Two antibodies, linked onto PSi and AuNPs, were used against different epitopes of prostate specific antigen, the common conjugating marker for these antibodies. Under white light illumination the photocurrent increases with growing AuNP surface density. The gate voltage is effective in decoupling electron-hole pairs created at the nanostructured PSi interface. In turn, the main effect of the immune-assembled AuNPs is the optimization of charge transport through the surface. The analysis of the photocurrent shows an outstanding spectral selectivity in the  $980 \pm 50$  nm NIR bandwidth. This report underlines the potential of the insertion of immune-assay protocols for the development of optoelectronic devices.

**Keywords:** immuno-assembly, sandwich assay, porous silicon, gold nanoparticles, phototransistor, optoelectronics.

## 1. Introduction

Challenges in the design of new generation phototransistors include the definition of active spectral windows (especially for the infrared range), miniaturization toward the formation of image pixels and more efficient devices with reduced energy consumption [1]. These challenges have been almost exclusively addressed using traditional solid state electronics. However, there is a current and increased tendency to turn towards the inclusion of photoactive biomolecules through soft processes [2, 3].

Phototransistors have been interlinked with the biological world at two different levels. First, for biomedical applications, including bioimaging and biosensing, the link relies on a signal exchange [4, 5]. For instance, wireless communications can be implemented in biosensors using a LED –phototransistor interface, which is commonly activated by an enzymatic reaction [6]. Second, a physical interfacing has been developed by the effective integration of photoactive biomolecules playing a photoconversion role [7, 8]. This trend towards the “natural” photosensitization of optoelectronic devices has been recently reviewed [7]. In this frame, the progress in organic and hybrid phototransistors is based on mimicking photon-sensitive biological circuits and has a specialized niche in the development of flexible, large area electronics for wearables and body-adaptive devices [3, 9, 10].

A third type of interlinking consists in the use of biomolecular interactions to assemble nanostructures with final functionality out of the biological/biomedical fields. The so derived superstructures have been designed by using alternatively DNA [11] or antigen-antibody [12] driven interactions. In this latter framework, the specific interactions of biomolecules are used to optimize 1D, 2D or 3D nanoconstructs where biomolecules play an

assembling role [13, 14]. Such architectures behave as bioengineered optical [15] and electronic devices [11, 16].

In the present work, we describe an immune-driven process for the sensitization of field-effect phototransistors, which is illustrated in Figure 1. A sandwich assay based on two specific antibodies against different epitopes of prostate specific antigen (PSA) [13] was used as a tool to quantitatively attach gold nanoparticles (AuNPs) to the surface of porous silicon (PSi). The dosage is regulated by the concentration of the PSA marker for a fixed concentration of AuNPs [17], which makes the process relatively “kinetics independent” if compared with processes promoting direct binding between surfaces and nanoparticles. PSA (also known as hK3) is a glycoprotein from the family of kallikreins, which exhibit enzymatic activity in some of their isoforms [18]. The presence of four sugar domains provides the molecule with strong hydrophilic character and prevents the formation of PSA isomers, but not its immune recognition. This is relevant from the point of view of physical properties, such as long range conductivity, very often related to isomeric structures conforming  $\beta$  sheets or  $\alpha$ -helices [19]. This is perfectly compatible with a short range electron transfer and/or transport in PSA (i.e. for enzymatic activity), but suggest that AuNPs could be effective surface enhancers of the surface conductivity on the device [20].

The presence of two surface and one back electrodes on the PSi/Si structure allows configuring a field-effect transistor in which the surface conductivity is regulated by the density of AuNPs attached to PSi (See Figure 1 and Experimental section for details) [17]. The photoconversion ability of PSi has previously allowed designing photon-sensitive devices [21-27]. Here we explore how the immunologically regulated surface density of AuNPs allows improving the overall performance of the PSi phototransistors.

## 2. Results and discussion

### 2.1. Phototransistor assembly and characteristics

Field-emission scanning electron microscopy was used to analyse the most critical assembly steps of the immune reaction induced phototransistor. The presence and concentration of AuNPs on the PSi surfaces was monitored in perspective view. The agreement of the expected AuNP size with nominal specifications was first monitored by UV-vis spectrometry (Figure S1). The main image in Figure 2.a shows a random distribution of AuNPs assembled on the PSi surface with marker concentrations of 10 ng/mL. The image shows that the AuNPs appear as isolated particles with mean separation distances of 1.6  $\mu\text{m}$  and no tendency to agglomeration, as derived from the low concentration colloidal solutions used during the assembly assays. The inset image shows a magnification of a 100 nm spherical AuNP on top of PSi, which exhibits the characteristic nanoroughness, not drastically affected by the biofunctionalization cascade.

To illustrate the optoelectronic properties of the immune-assembled PSi-AuNPs devices we carried out two different types of measurements for the samples under illumination. Figure 2.b shows the source-drain characteristics ( $I$  vs  $V_P$ ) measured across the two NiCr electrodes disposed on the PSi surface for the sample assembled with a 10 ng/mL solution of PSA for different values of the gate voltage ( $V_G$ ) applied through the back Al contact. The presented curve is representative of the curves obtained with three different replicas showing  $\pm 5\%$  current deviations at -1 V  $V_P$ . The results demonstrate an increasing influence of the fourth quadrant contribution for increasing gate voltage, which evidences a reverse light-induced current. The changing trends of the curves denote the presence of different transport mechanisms. Such conduction transitions are well known in PSi-based

optoelectronic devices and are attributed to different tunnelling conduction regimes [28-31]. However, the remarkable changes in the concavity of the curves, as specially identified for the curve corresponding to a gate voltage of 2.5 V (from a polarization voltage of -0.25 V to positive values) suggest the presence of leakage currents. In other words, the gate voltage is effective in enhancing the reverse current, although leaking currents counteract part of the effect.

The relevance of an increasing density of surface immobilized AuNPs on the generated photocurrent is shown in figure 2.c for a  $V_G$  voltage of 2.5 V. The figure shows clearly (follow the control sample curve) the presence of a photocurrent even without specifically immobilized AuNPs. The photocurrent is improved by the gradual increase of surface AuNPs, with a remarkable increase of the efficiency after incorporation of AuNPs using 10 ng/mL PSA.

We further studied the behaviour of the phototransistor prototypes in a diversity of on-off configurations. We firstly studied the response of the devices with different AuNPs surface densities to the light stimuli by maintaining constant feed conditions. Figure 2.d) shows the dark to light transitions for constant operation with  $V_G=V_P= 0.5$  V. The curves were obtained from a full dark state passing to a pulsed light state (5 s On+ 5 s Off pulses). The curves show that a few cycles are necessary to reach a steady operation. It can be observed that, the higher the concentration of AuNPs, the longer it takes to reach a steady operation. This overall time to steady operation is determined by the raise of current at each light-on transition. It can be noted that, while the current derivative just before the on-off transition is zero (or almost zero) for samples with low density of AuNPs, this derivative is still highly positive for the samples with higher density of AuNPs (especially for 10 ng/mL). The overall raise in the off to on current is observed to increase non linearly for devices with

increasing density of AuNPs. However, the increase of net transported charge is accompanied by an increase in the overall time required for reaching a steady operation, which suggests again that counteracting transport processes take place within the network of AuNPs. This suggests once more that the light-off current level is induced by leaking currents. To confirm this issue, this light-off current could be effectively shut down to zero when the gate voltage is null, as illustrated in the gate On-Off vs time characteristics of figure S2.

## 2.2. Photocurrent and photoresponsivity

Photocurrent measurements were performed in order to determine the active spectral regions of the devices. The measurements were performed at  $V_G = V_P = 0$  V in order to avoid the effects of leaking currents. Additionally, in order to take into account the effect of the light source, the photoresponsivity was determined according to equation [32]:

$$R = \frac{I_P - I_d}{P \cdot S} \quad (1),$$

where,  $I_P$  is the photocurrent,  $I_d$  is the dark current,  $P$  is the incident power density and  $S$  is the active area of the device ( $1.23 \text{ cm}^2$ ). Figure 3.a depicts such photo-response for the devices prepared with different density of AuNPs. The results show that the spectral active region starts at 890 nm for all the devices. The extinction wavelength is reached after the decay of the peak tail at 1150 nm. The energy associated to the light providing the threshold current is 1.4 eV and the value corresponding to the maximum peak is 1.27 eV, which are in good agreement with typical values of the band gap for Si nanostructures within PSi [26]. The pseudo-Gaussian photocurrent peak suggests the presence of a non-homogeneous distribution of Si quantum dots within PSi, with band-gap values ranging from circa 1.4 eV down to the bulk value of 1.1 eV for the Si wafer (related to the extinction signal



wavelength of circa 1150 nm). Relevantly, the photocurrent peak reveals a remarkable growth for increasing amounts of AuNPs. These results confirm again a relevant role of the AuNPs in the transport of the photogenerated current, plausibly created from electron-hole pairs generated within PSi.

The potential influence of a near field contribution from irradiated AuNPs to the photocurrent does not look plausible. In fact, we considered the spectral shifts for near field contributions of AuNPs of 100 nm diameter due to their changing refractive index environment after assembling on PSi. The simulations took into account an organic coating onto both PSi and AuNPs and a permeation parameter ( $h$ ) regulating the position of the bottom of the AuNP with respect to the PSi surface (see figure S3). However, the maximal expected spectral shift reaches only +20 nm for nanoparticles with considerable permeation in the PSi structure, which is far apart the spectral-active region of the devices.

Finally, we analysed the overall photoresponsivity of the devices in a set of different configurations. Figure 3.b shows a histogram of the photoresponsivity for  $V_P = V_G = 0.5$  V. The histogram is well in agreement with previous results on photocurrent generation [33]. The values obtained show quite low photoresponsivity, which is mainly due to the restricted spectral-active region of the devices. If the photoresponsivity is redefined considering only the power emitted by the light source from the 890 nm edge, the photoresponsivity values increase by 80 % with respect to plotted values for the whole spectral range, reaching values of 20 mA/W for the 10 ng/mL devices at the low operation potentials of 0.5 V.

### **2.3. Device operation**

The previous results suggest that the origin of the photocurrent is induced by generation of electron-hole pairs in Si nanostructures, which can be effectively separated by

increasing gate voltages. The negative voltage bias applied to the Al electrode is responsible of creating an electric field, which increases to the bottom of the PSi structure, and screens electrons to the PSi surface. This transition from zero to negative gate bias is illustrated in the band diagrams of figure 4.a (top to middle), where PSi has been considered with a mean band gap of 1.3 eV. In this situation, by connecting one of the surface NiCr electrodes to ground, it is possible to collect a current at null polarization voltage between the NiCr surface electrodes, which is identified in figure 2.a by the crossing of the curves with the ordinate axis.

By generating a surface potential difference between the two NiCr surface electrodes, free electrons are preferentially directed to the positive NiCr electrode and their confinement induces recombination of electron-hole pairs, which diminishes the collected current. Additionally, even though an increasing gate voltage is favourable in separating electron-hole pairs, at high gate voltage, holes can get injected into bulk Si and recombine with electrons provided by the negative gate bias, inducing a leak current, which is responsible for the concave shape of the characteristic curves at the fourth quadrant. This situation of high negative voltage inducing leak through recombinations at the Si/PSi interface is illustrated in the third band diagram of figure 4.a (bottom).

At surface level, a homostructure composed of nanostructured PSi is sandwiched between the NiCr electrodes (figure 4.b, top). The porous and composite nature of PSi (porous silica matrix with embedded Si quantum dots) makes the widened band tilt under a surface polarization [34]. The applied voltage facilitates the extraction of charge as illustrated in the band diagram of figure 4.b middle. The role of AuNPs can be interpreted in such band structure as a local short-circuit, which makes charge transport more effective since the path to the drain electrode becomes shorter and the mean electric field on PSi is slightly increased.

However, the increase in the transport efficiency by an increasing density of AuNPs is also accompanied by a higher electron-hole recombination rate. This explains the increasing concavity of the I-V curves in the fourth quadrant of Figure 4.b for increasing density of AuNPs.

In fact, this recombination current becomes dominant for  $V_P > V_G$  and leads to the behaviour of the I-V curves in the first quadrant, which present much higher currents for high doses of AuNPs. Thus, the main effect of the AuNPs is the optimization of transport of carriers through the surface electrodes. To illustrate this graphically, we have plotted the current at  $V_P = 0$  V and  $V_G = 2.5$  V and the maximum photocurrent at  $V_P = V_G = 0$  V as a function of the surface dosage of AuNPs (see figure 4.c, right and left axis, respectively). The results illustrate that the effect of current improvement is consistent, but is accompanied by a decrease in the improvement rate for each increment of the AuNPs dosage.

### 3. Conclusion

We have demonstrated that a sandwich assay allows the controlled integration of AuNPs on the surface of PSi-based field effect phototransistors. The experimental results suggest that the presence of silicon quantum dots in PSi is responsible of generating electron-hole pairs under illumination. These can be converted into a photocurrent, which is greatly amplified by the application of a negative gate voltage. The photocurrent is also drastically affected by the surface density of AuNPs, which actuate as an effective current amplifier by reducing the probability of electron-hole recombinations. Control experiments confirm that the response of PSi to unspecifically bound AuNPs is negligible with respect to those immobilized through PSA directed recognition. The devices are responsive in the  $980 \pm 50$

nm spectral range, in agreement with the presence of Si quantum dots with a mean bandgap of 1.3 eV. The responsivity at very low gate and polarization voltages of 0.5 V reaches values of 20 mA/W, considering the incident light within the spectral active window of the devices.

These results open the path to the controlled integration of other types of nanoparticles on different types of field effect transistors for the optimization of their optoelectronic behaviour. In overall, the present work highlights the technological value of biotechnological processes for the improvement of optoelectronic architectures.

## 4 Experimental

### *Porous silicon phototransistor*

PSi was prepared on [100] p-type (B doped) Si wafers with 0.05–0.1  $\Omega\cdot\text{cm}$  resistivity. The back-side was coated with an Al film by e-beam evaporation and annealed by rapid thermal processing (400°C, N<sub>2</sub> atmosphere) to form a low resistance ohmic contact. 15 × 15 mm<sup>2</sup> Si pieces were then mounted into a Teflon protected electrochemical anode. A sponge-type PSi was formed by the anodic etching of the silicon wafer in hydrofluoric acid (HF) absolute ethanol (EtOH) electrolytes at volume ratios of 1:1. The PSi film formed with a constant current density of 80 mA/cm<sup>2</sup> during 20 s presented a mesoporous structure and a thickness of 1  $\mu\text{m}$  [35]. The formed PSi was neutralized with ethanol and dried under N<sub>2</sub> flow.

Corrosion resistant Ni/Cr surface contacts were subsequently grown on PSi. Two void slots were first etched in PSi by Ar<sup>+</sup> beam milling (0.5 keV, up to 0.6 C total charge) through a Si mask [17]. Ni/Cr contacts were then deposited in the 250 nm deep slots using 40/60 Ni/Cr wt % targets for sputtering with a magnetron fed at 0.5 kV, 1 A and working pressure

of  $10^{-2}$  mbar. Figure 1.a presents schematically the basic configuration of the PSi device with its back (Al) and top (NiCr) electrical contacts.

#### *PSi-AuNPs immunoassembly*

The formation of the PSi/AuNP assemblies required a first step of PSi organo-silanization. After a soft surface peroxidation of PSi in  $\text{H}_2\text{O}_2/\text{EtOH}$  at 1:1 volume fraction, an epoxy-silanization at room temperature for 1h with (3-Glycidyloxypropyl)trimethoxysilane (GPTMS, Sigma-Aldrich) in methanol at 1:1000 volume ratio was considered as an efficient way to functionally immobilize the antibodies [36]. The silanization takes place spontaneously by a condensation reaction between the surface silanol (SiOH) groups on PSi and the three hydrolysable trimethoxy groups of GPTMS. The GPTMS molecule and this surface activation step are schematically represented in figure 1.b.

A capture antibody (monoclonal mouse anti-PSA 1H12 antibody, 50  $\mu\text{g}/\text{mL}$ , HyTest, Turku, Finland) was then immobilized for 2 h at  $37^\circ\text{C}$  using the GPTMS epoxy ligands in 10 mM 2-morpholinoethanesulfonic acid (MES) (pH 3.8). This step is depicted schematically in figure 1.c. Prior to recognition with the antigen (PSA), non-specific interactions were inhibited by blocking the GPTMS-PSi surface overnight at  $4^\circ\text{C}$  with aminoethyl-polyethylene glycol (PEG) (Sigma-Aldrich) at 1 mg/mL in 10 mM MES and 0.05% Tween<sup>®</sup> (pH 5.5). The first immunoreaction between PSA (antigen) and the immobilized 1H12 antibody took place at  $37^\circ\text{C}$  for 2 h in fetal bovine serum (FBS) 1x competitive conditions. PSA (HyTest, Turku, Finland) concentrations from 100 pg/mL to 10 ng/mL were considered

using logarithmic increments, which were compared with a negative PSA control. This step is represented schematically in figure 1.d.

Spherical AuNPs of 100 nm diameter and coated with 2-3 nm long carboxyl-thiol-spacer (C11-100-TC-50, Nanopartz<sup>TM</sup>) were selected for integration on PSi. The nanoparticles were pre-characterized by UV-vis spectroscopy. The results shown in figure S1 show that the experimental extinction spectrum is in good agreement with theoretical extinction spectra obtained from Mie scattering theory. Optical properties of Au were extracted from McPeak et al. [37]. The coupling of the AuNPs with the PSi surface was also simulated through a Finite-Difference Time-Domain (FDTD) method using Lumerical Software and optical data for Au [37] and PSi [38]. The AuNPs were conjugated with a PSA detection antibody (anti-PSA 5A6 antibody, HyTest, Turku, Finland) in MES (pH 3.8) with 0.05% Tween [39]. The binding of the AuNPs to PSi was carried out through a 5A6/PSA/1H12 sandwich by immersion for 1h at 37°C with a 5 µg/mL 5A6-AuNPs solution as depicted schematically in figure 1.e. For statistical purposes, five replica samples were produced for each different biofunctionalization condition. The morphology of the surfaces and interfaces was studied by field emission scanning electron microscopy (FESEM) using a Philips XL-40FEG microscope operated at 3.0 kV. Interparticle distance analysis was carried out using the measurement module implemented in ImageJ [40].

#### *Photoelectrical characterization*

The optoelectronic characterization of the PSi-AuNPs phototransistors was performed by measuring under illumination their I-V characteristics (SP-150 instrument, Bio-Logic Science) between the top source-drain interdigitated electrodes while applying a given voltage to the Al gate contact (Keithley 2400 SourceMeter). The basic scheme for the

measurements is illustrated in figure 1.f. An electrical measurements cell consisting of two copper surface pin probes and a copper base ( $2 \text{ cm}^2$ ) located in a Faraday box was used. Details of the different measurements are described in the following paragraphs.

I-V measurements of NiCr/PSi/Si/Al structures were carried out under dark conditions in a Faraday box to shield them from any external interfering signals. The applied potential ranged between +2 and -2 V with a scan rate set to 20 mV/s. The photoresponse of the fabricated phototransistors was examined using two light sources with different power intensity, (0.2 and 2 mW). The first experiment, (I-V curves) was performed using a phosphorescent white light source (0.2 mW) for the control sample and samples with different concentrations of AuNPs (100 pg/mL, 1 ng/mL and 10 ng/mL). The I-V measurements were carried out in the polarization voltage ( $V_P$ ) range from -1 to 3.5 V with a constant gate voltage ( $V_G$ ) equal to 2.5 V. The On-Off experiments used pulsed light (2 mW) at a constant  $V_P = V_G = 0.5 \text{ V}$ , the current recorded with current steps of 2  $\mu\text{A}$  and a sampling time set to  $dt = 0.15 \text{ s}$ . The distance between the measured samples and the light source has been set to 15 cm. The estimation of the photoresponse stability of the devices has been estimated by measuring (I-t) curves for 2 minutes.

To study the response of the devices to the external gate voltage ( $V_G$ ), I-V curves for sample 1 ng/mL were measured out in the  $V_P$  range from +2 to -2 V with different applied  $V_G$  voltage from 0 V to 2 V, with steps of 0.5 V. ON/OFF external voltage response was carried out at constant  $V_P = V_G = 0.5 \text{ V}$  for all the fabricated devices under dark conditions. The current was recorded for 2 minutes with current steps of 2  $\mu\text{A}$  and a sampling time set to  $dt = 0.15 \text{ s}$ .

Photocurrent measurements were carried out at 0 V bias using a dual digital lock-in amplifier (Signal Recovery 7225) at a chopper frequency of 350 Hz. Illumination was

provided by an Acton Research Corporation Tungsten-Deuterium dual light source (model TDS-429) and a SpectraPro 150 monochromator equipped with three interchangeable diffraction gratings (1200 lines/mm) was used to select the wavelength. The photocurrent was recorded by moving the diffraction grating every 2 nm.

## **Acknowledgements**

Authors thank Luis García Pelayo for technical assistance during materials processing and characterization. The current research was funded by grant SPECTRASENSE, RTC-2017-6311-1 from the Government of Spain.

## **Data availability**

The raw/processed data required to reproduce these findings cannot be shared at this time due to technical or time limitations.

## **References**

- [1] S. Bianconi, H. Mohseni, Reports on Progress in Physics 83 (2020).
- [2] C. Wang, X.T. Zhang, W.P. Hu, Chemical Society Reviews 49 (2020) 653-670.
- [3] N. Li, Z.J. Lan, L.F. Cai, F.R. Zhu, Journal of Materials Chemistry C 7 (2019) 3711-3729.
- [4] G. Chaji, A. Nathan, Q. Pankhurst, Applied Physics Letters 93 (2008).
- [5] Y.W. Chang, Y.T. Tai, Y.T. Huang, Y.S. Yang, Ieee Sensors Journal 9 (2009) 673-677.
- [6] T. Hanashi, T. Yamazaki, W. Tsugawa, S. Ferri, D. Nakayama, M. Tomiyama, K. Ikebukuro, K. Sode, Biosensors & Bioelectronics 24 (2009) 1837-1842.
- [7] H.A. Maddah, V. Berry, S.K. Behura, Renewable & Sustainable Energy Reviews 121 (2020) 25.
- [8] L. Frolov, Y. Rosenwaks, S. Richter, C. Carmeli, I. Carmeli, Journal of Physical Chemistry C 112 (2008) 13426-13430.



- [9] G.F. Jones, R.M. Pinto, A. De Sanctis, V.K. Nagareddy, C.D. Wright, H. Alves, M.F. Craciun, S. Russo, *Advanced Materials* 29 (2017) 7.
- [10] X.H. Huang, D.Y. Ji, H. Fuchs, W.P. Hu, T. Li, *Chemphotochem* 4 (2020) 9-38.
- [11] A.V. Pinheiro, D.R. Han, W.M. Shih, H. Yan, *Nature Nanotechnology* 6 (2011) 763-772.
- [12] S.P. Wang, N. Mamedova, N.A. Kotov, W. Chen, J. Studer, *Nano Letters* 2 (2002) 817-822.
- [13] J.M. Nam, C.S. Thaxton, C.A. Mirkin, *Science* 301 (2003) 1884-1886.
- [14] E. Katz, I. Willner, *Angewandte Chemie-International Edition* 43 (2004) 6042-6108.
- [15] M.B. Ross, J.C. Ku, B. Lee, C.A. Mirkin, G.C. Schatz, *Advanced Materials* 28 (2016) 2790-2794.
- [16] Y. Wang, Z.Y. Tang, S.S. Tan, N.A. Kotov, *Nano Letters* 5 (2005) 243-248.
- [17] C. Rodriguez, V. Torres-Costa, O. Ahumada, V. Cebrian, C. Gomez-Abad, A. Diaz, M.M. Silvan, *Sensors and Actuators B-Chemical* 267 (2018) 559-564.
- [18] M.J. Ahrens, P.A. Bertin, E.F. Vonesh, T.J. Meade, W.J. Catalona, D. Georganopoulou, *Prostate* 73 (2013) 1731-1737.
- [19] N.L. Ing, M.Y. El-Naggar, A.I. Hochbaum, *Journal of Physical Chemistry B* 122 (2018) 10403-10423.
- [20] F. Zaibi, I. Slama, C. Okolie, J. Deshmukh, L. Hawco, M. Mastouri, C. Bennett, M. Mkandawire, R. Chtourou, *Colloids and Surfaces a-Physicochemical and Engineering Aspects* 589 (2020) 11.
- [21] L.Z. Yu, C.R. Wie, *Sensors and Actuators a-Physical* 39 (1993) 253-257.
- [22] L.A. Balagurov, D.G. Yarkin, G.A. Petrovicheva, E.A. Petrova, A.F. Orlov, S.Y. Andryushin, *Journal of Applied Physics* 82 (1997) 4647-4650.
- [23] M. Kruger, M.G. Berger, M. Marso, W. Reetz, T. Eickhoff, R. Loo, L. Vescan, M. Thonissen, H. Luth, R. ArensFischer, S. Hilbrich, W. Theiss, *Japanese Journal of Applied Physics Part 2-Letters & Express Letters* 36 (1997) L24-L26.
- [24] L.T. Canham, T.I. Cox, A. Loni, A.J. Simons, *Applied Surface Science* 102 (1996) 436-441.
- [25] F. Priolo, T. Gregorkiewicz, M. Galli, T.F. Krauss, *Nature Nanotechnology* 9 (2014) 19-32.
- [26] R. Ramadan, M. Manso-Silvan, R.J. Martin-Palma, *Journal of Materials Science* 55 (2020) 5458-5470.
- [27] V. Torres-Costa, R.J. Martin-Palma, J.M. Martinez-Duart, *Materials Science & Engineering C-Biomimetic and Supramolecular Systems* 27 (2007) 954-956.
- [28] H.P. Maruska, F. Namavar, N.M. Kalkhoran, *Applied Physics Letters* 61 (1992) 1338-1340.
- [29] D. Deresmes, V. Marissael, D. Stievenard, C. Ortega, *Thin Solid Films* 255 (1995) 258-261.
- [30] T. Ozaki, T. Oguro, H. Koyama, N. Koshida, *Japanese Journal of Applied Physics Part 1-Regular Papers Brief Communications & Review Papers* 34 (1995) 946-949.
- [31] D. Gallach-Perez, A. Munoz-Noval, L. Garcia-Pelayo, M. Manso-Silvan, V. Torres-Costa, *Journal of Luminescence* 191 (2017) 107-111.
- [32] D.Z. Yang, D.G. Ma, *Advanced Optical Materials* 7 (2019).
- [33] J.N. Deng, L.Y. Zong, M.S. Zhu, F.Y. Liao, Y.Y. Xie, Z.X. Guo, J. Liu, B.R. Lu, J.L. Wang, W.D. Hu, P. Zhou, W.Z. Bao, J. Wan, *Advanced Functional Materials* 29 (2019) 9.
- [34] A. Onipko, L. Malysheva, *Physical Review B* 64 (2001).

- [35] N. Naveas, V. Torres Costa, D. Gallach, J. Hernandez-Montelongo, R.J. Martin Palma, J. Predenstinacion Garcia-Ruiz, M. Manso-Silvan, Science and Technology of Advanced Materials 13 (2012).
- [36] C. Rodriguez, P. Dietrich, V. Torres-Costa, V. Cebrian, C. Gomez-Abad, A. Diaz, O. Ahumada, M.M. Silvan, Applied Surface Science 492 (2019) 362-368.
- [37] K.M. McPeak, S.V. Jayanti, S.J.P. Kress, S. Meyer, S. Iotti, A. Rossinelli, D.J. Norris, Acs Photonics 2 (2015) 326-333.
- [38] V. Torres-Costa, R. Gago, R.J. Martin-Palma, M. Vinnichenko, R. Grotzschel, J.M. Martinez-Duart, Materials Science & Engineering C-Biomimetic and Supramolecular Systems 23 (2003) 1043-1046.
- [39] P.M. Kosaka, V. Pini, J.J. Ruz, R.A. da Silva, M.U. Gonzalez, D. Ramos, M. Calleja, J. Tamayo, Nature Nanotechnology 9 (2014) 1047-1053.
- [40] W.S. Rasband, ImageJ, U. S. National Institutes of Health, Bethesda, Maryland, USA, 1997-2018, p. <https://imagej.nih.gov/ij/>

## Figures and Captions

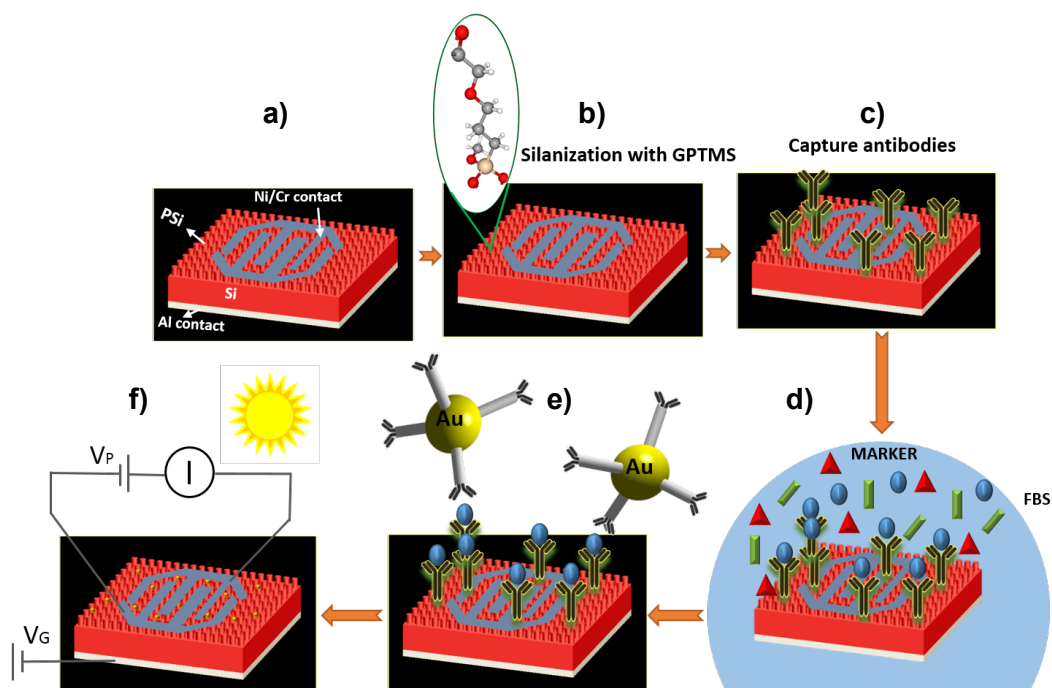


**Figure 1.** Fabrication scheme of the PSi-AuNPs phototransistor: a) Ion beam and plasma sputtering processing of the NiCr source-drain electrodes. b) organo-silanization with (3-Glycidyloxypropyl)trimethoxysilane (GPTMS, chemical structure inset). c) Immunoassembly first stage: immobilization of the capture antibody on PSi. d) Immunoassembly second stage: recognition of the PSA marker. e) Immunoassembly third stage: sandwich with gold-detection antibody conjugate. f) Determination of phototransistor response.

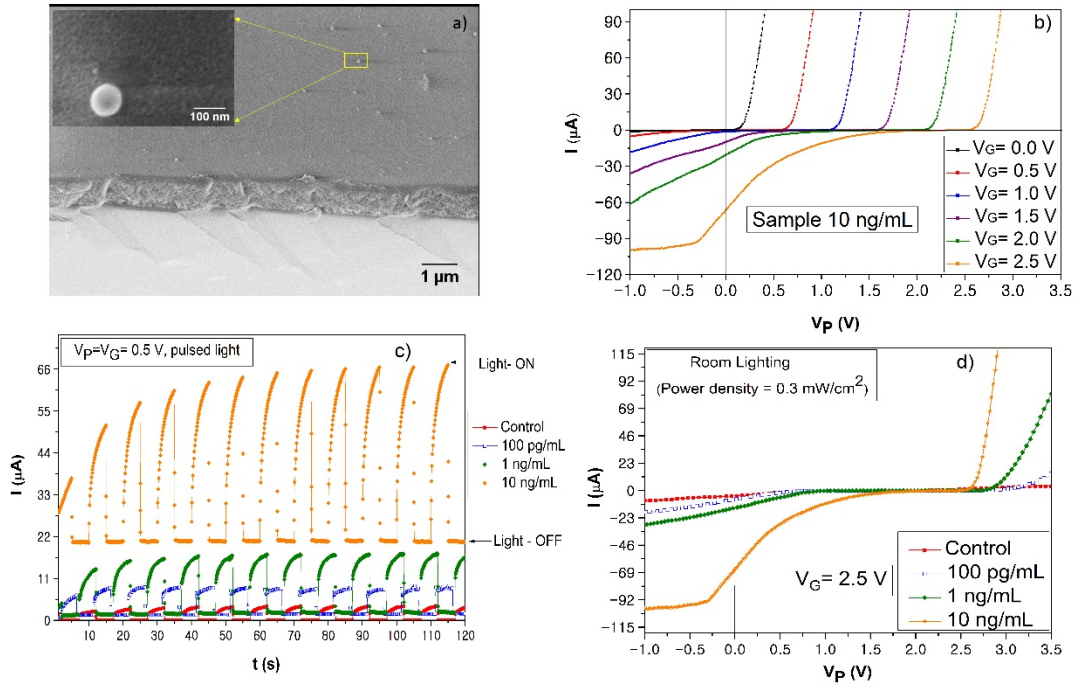


**Figure 2.** a) FESEM images from the surfaces of AuNPs/PSi devices loaded with 10 ng/mL AuNPs. I- $V_P$  characteristics of the PSi-AuNPs phototransistors at room lighting (0.3 mW/cm<sup>2</sup>): b) at different gate voltages ( $V_G$ ) for a single concentration of AuNPs (10 ng/mL) and, c) for different concentrations of AuNPs at a common gate voltage  $V_G = 2.5$  V. d) White-light (2.85 mW/cm<sup>2</sup>) On-Off characteristics for the devices with different concentrations of AuNPs and  $V_G = V_P = 0.5$  V.

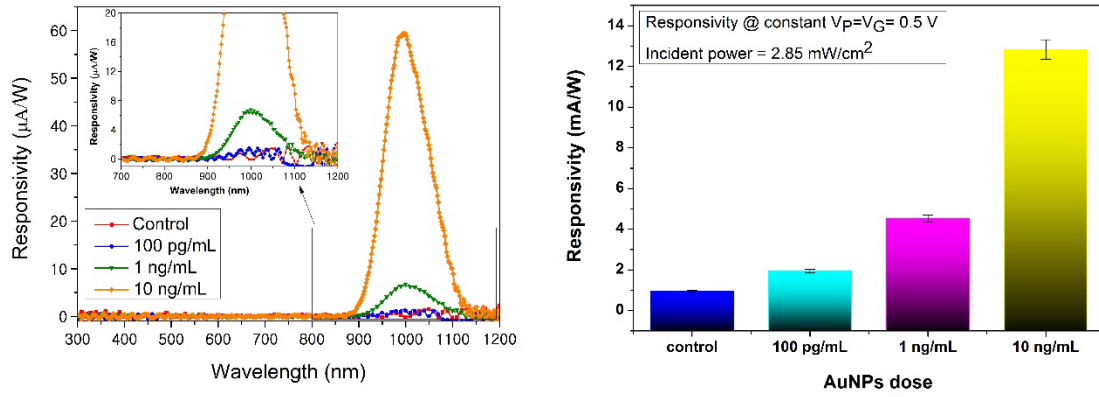


**Figure 3.** a) Responsivity of obtained from spectroscopic photocurrent measurements for the phototransistors with different concentrations of AuNPs and  $V_G=0\text{ V}$ . b) Evolution of PSi photoresponsivity for increasing concentrations of AuNPs with measurements at  $V_P = V_G = 0.5\text{ V}$  and a light incident power of  $2.85\text{ mW/cm}^2$ .

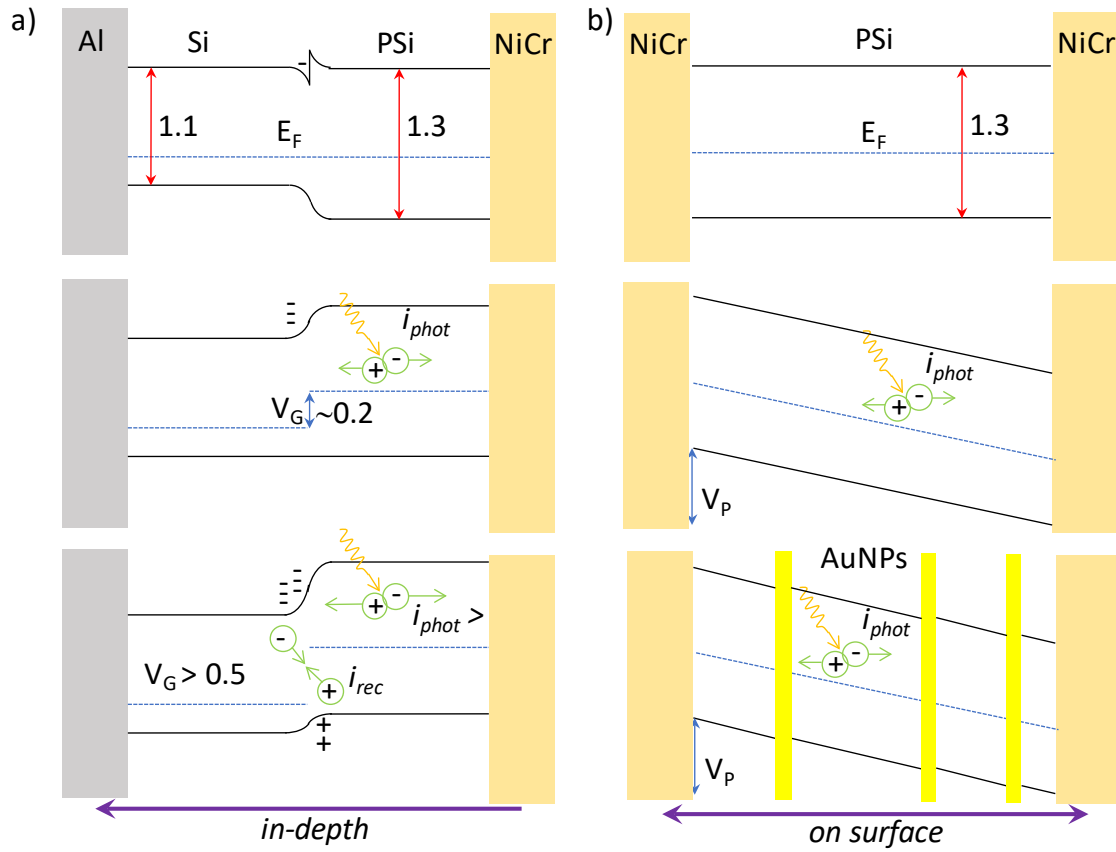


**Figure 4.** a) Band diagram associated to the Al/Si/PSi/NiCr structure in the dark (top), under illumination at  $V_G = 0.2$  V (middle) and under illumination at  $V_G > 0.5$  V (bottom). b) Band diagram associated to the NiCr/PSi/NiCr structure in the dark (top), under illumination and surface polarization ( $V_P$ ) (middle) and, under illumination and surface polarization ( $V_P$ ) in the presence of AuNPs.

## Supplementary material

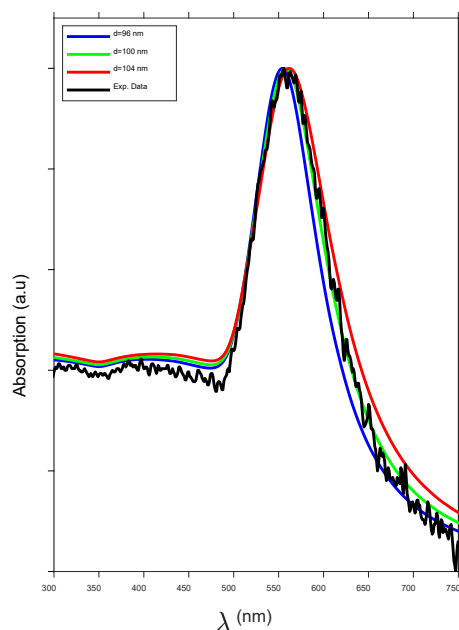


**Figure S1.** Extinction spectra in water obtained from Mie scattering theory of spherical AuNPs with different diameter in comparison with the experimental extinction spectrum of the AuNPs of nominal size of 100 nm used in this work (black line).

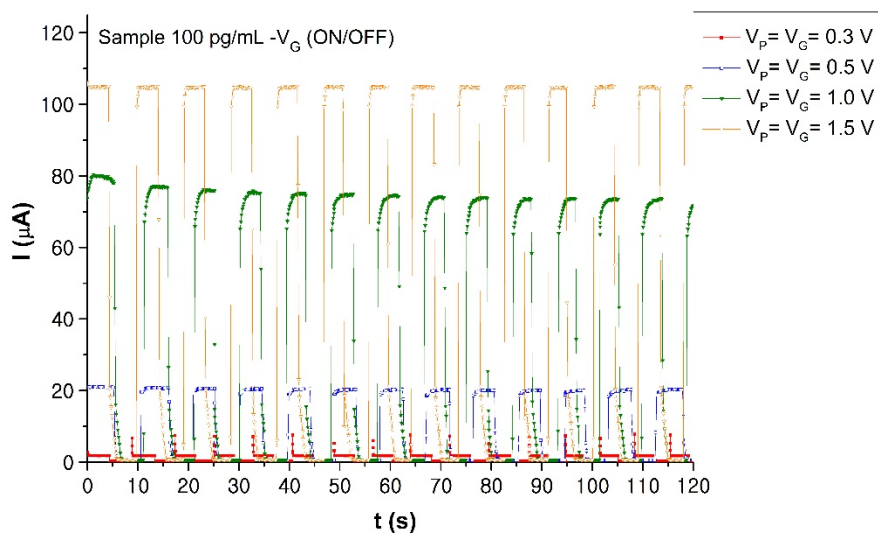


**Figure S2.** Gate voltage on-off characteristics for the sample incubated with GNPs at the PSA concentration of 100 pg/mL for different values of  $V_G$  ( $V_G = V_P$ ).

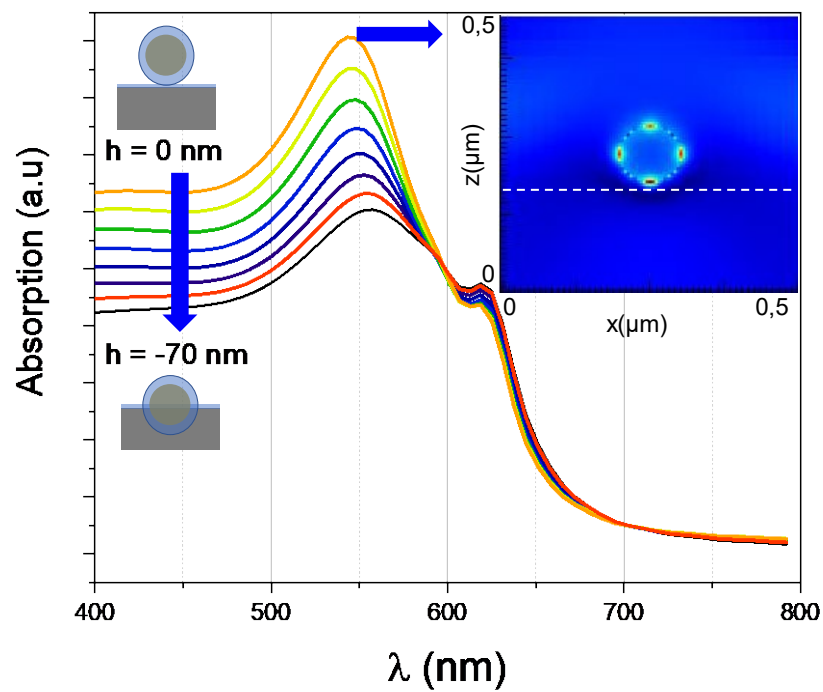


**Figure S3.** Absorption spectra calculated with Mie scattering theory for functionalized 100 nm diameter AuNPs with an organic coating ( $n = 1.4$ ) of 5 nm in air and with different permeation levels ( $h$ ) within the PSi substrate. Inset: Intensity of the electric field at quadrupolar mode at 540 nm and  $h = 0$  nm.